CHEMISTRY OF MATERIALS

ARTICLE

pubs.acs.org/cm

Study on the Defect Structure of SnO_2:F Nanoparticles by High-Resolution Solid-State NMR

Yamini S. Avadhut,[†] Johannes Weber,[†] Elin Hammarberg,[‡] Claus Feldmann,[‡] Inga Schellenberg,[§] Rainer Pöttgen,[§] and Jörn Schmedt auf der Günne*[,†]

[†]Department of Chemistry, Ludwig-Maximilians-Universität München, Butenandtstrasse 5-13 (D), D-81377 München, Germany

[‡]Institut für Anorganische Chemie, Karlsruhe Institute of Technology (KIT), Engesserstrasse 15, D-76131 Karlsruhe, Germany

[§]Institut für Anorganische und Analytische Chemie, Universität Münster, Corrensstrasse 30, D-48149 Münster, Germany

Supporting Information

ABSTRACT: In this contribution the preparation and structural characterization of nanoscale fluorine doped tin-oxide (SnO_2:F, FTO) is described. By using a microwave assisted polyol approach, nanoparticles with different doping levels are prepared, which show narrow size distribution as measured by X-ray diffraction, electron microscopy and dynamic light scattering. They were converted into electrically conductive optically transparent films at 500 °C by a specific thermal treatment (500 °C in air followed by 250 °C in forming gas), exhibiting a specific resistivity of (1.9×10^{-1} Ω cm). Solid-state MAS NMR and ^{119}Sn Mössbauer spectroscopy were used to study how F atoms are incorporated into the SnO_2:F nanoparticles. Distance constraints were determined by ^{119}Sn{^{19}F} REDOR, fluorine-doping homogeneity by homonuclear dipolar recoupling experiments ($SR6_6^2$). Cross-polarization was used to investigate the immediate environment of the dopant. The experiments were supplemented by first-principles quantum-chemical calculations for possible defect site models. The combined data strongly indicate that F doping is not directly related to an increase in charge-carrier concentration, even though F atoms do occupy O vacancy sites in SnO_2:F. For this study we have implemented background compensated NMR 2D pulse-sequences which reliably suppress the fluorine background originating from the NMR probe. Moreover we show that cluster calculations on the basis of the extended embedded ion method (EEIM) can be used to study the structure of diluted defects in crystalline host structures and predict NMR properties.

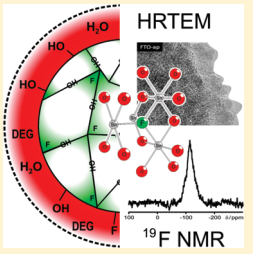

KEYWORDS: fluorine-doped tin-oxide, nanomaterial, synthesis, noncrystalline, solid-state NMR, transparent conductive oxide, TCO, defect structures, first principles calculations

INTRODUCTION

Metal oxides that exhibit high optical transmittance and in addition high electrical conductivity are referred to as transparent conductive oxides (TCOs).[1] They can also be described as wide-band gap oxide semiconductors[2] serving a wide range of applications.[3−5] Examples of compounds within this material class are CdO, In_2O_3, SnO_2, and ZnO. If such an oxide is suitably doped, high electrical conductivities can be achieved.

Among the transparent conductive oxides, tin-doped indium oxide, also called indium tin oxide (ITO), currently shows the highest electrical conductivity, which in combination with its optical transmittance has granted it a position as the most widely applied TCO material in optoelectronic devices.[6,7] However, because of the high cost and scarcity of indium, intense research to find materials that can replace ITO is conducted. Among the possible substitutes for ITO is fluorine-doped tin oxide (SnO_2:F, alias FTO), which is a n-doped oxide[8] employed for coating energy-efficient windows.[5,9]

SnO_2:F films are commonly produced via vacuum-based gas-phase methods, such as magnetron sputtering[4,5] and structured thereafter via lithographic etching. Because this conventional procedure involves time-consuming and cost-intensive steps, coating or printing techniques (e.g., dip- or spin-coating, inkjet, offset or silk screen printing) would be much more favorable. In addition, they could be applied for printing on flexible substrates (e.g., plastic and paper).[10,11] Printing techniques, however, essentially require suitable suspensions or inks, containing crystalline nonagglomerated, SnO_2:F nanoparticles.

Liquid phase methods for the preparation of nanoparticles include water-based precipitation,[12,13] sol−gel synthesis,[9,14−16] microemulsion techniques,[9,17] as well as hydrothermal[9,18] and solvothermal[9,19] methods. In this work, a polyol-mediated approach is applied to the synthesis of SnO_2:F.[20,21]

Although numerous works investigating nanostructured materials focused on empirical tuning of their physical and chemical properties,[9,12,13] we believe there is a lack of understanding how synthesis, structure and properties are related. The latter often differ significantly from those of bulk materials of similar composition. Structural analysis of bulk crystalline materials is well established but structural analysis of nanoparticles is still developing and requires characterization of defects, static/dynamic disorder and intra- and interparticle interfaces. For

Received: November 15, 2010
Revised: January 24, 2011
Published: February 22, 2011

example, bulk TCO materials are believed to be limited in their electrical conductivity through ionized impurity scattering,[22] whereas for nanoparticles supposedly scattering at various defects (intra-, interparticle interfaces) is the conductivity bottleneck;[23,24] however, the analytical basis for these models is rather limited.

Individual nanoparticles can be monocrystalline, amorphous or "polycrystalline", in the sense of having several domains in an individual particle, where each of these domains is monocrystalline and where at the junction between different domains the above-mentioned intraparticle interfaces exist. Here we use solid-state NMR to characterize such interfaces of polycrystalline nanoparticles. Relevant NMR experiments are heteronuclear double-resonance experiments like HARDSHIP[25] and different flavors of the REDOR experiment,[26] which have already been used to characterize the core−shell structure of nanoparticles. These experiments are sensitive to long-range heteronuclear interactions in the nanometer range because the heteronuclear dipolar interactions of a core nucleus *I* are simultaneously recoupled to all nuclei *S* in the shell/intraparticle interface.

With respect to the nature of an individual point defect in a doped nanoparticle, magnetic resonance offers several techniques to probe its short-range structure, for example ^{119}Sn Mössbauer spectroscopy,[27] ^{119}Sn, ^{17}O, ^{1}H, and ^{19}F NMR,[28] which can be confronted with calculated chemical shift values[29,30] coming from structural models. Mössbauer spectroscopy allows to access the electron density at the tin atom and the valence state of tin, i.e., Sn(0), Sn(II), Sn(IV). At the particle surface, hydrogen will play an important role to saturate dangling bonds, so that two isotopes ^{1}H and ^{19}F are available which offer enough sensitivity to elucidate structural details by more sophisticated NMR experiments.

The particles in this study aim at nanocrystalline fluorine-doped tin oxide SnO_2:F which are prepared by the polyol-method in diethylene glycol being followed by a thermal treatment in forming gas. Particle size and distribution are characterized by several independent analytical tools, namely electron microscopy (SEM, TEM), X-ray powder diffraction (XRD), and dynamic light scattering (DLS). Electrical DC conductivity on pressed powder pellets is reported at the various stages of the synthetic process.

EXPERIMENTAL SECTION

Synthesis. *Polyol-Mediated Synthesis.* In a typical recipe, 5.7 mmol of $SnCl_4 \cdot 5H_2O$ and 0.057 mmol of $N(CH_3)_4F \cdot 4H_2O$ or 0.57 mmol of $N(CH_3)_4F \cdot 4H_2O$ were dissolved in 50 mL of diethylene glycol (DEG). At 80 °C this solution was added to a solution of 50 mL DEG containing 28.5 mmol $N(CH_3)_4OH \cdot 5H_2O$ and 2 mL of deionized H_2O. Upon adding both solutions, no precipitation occurred. As the mixture was heated to 200 °C in a standard laboratory microwave oven (MLS rotaprep: 1200 W, 2.45 GHz; fiber optic as well as pyrometer for temperature control; magnetic stirrer), precipitation was observed. To improve materials crystallinity, the temperature was maintained for 1 h. During irradiation, the sample was continuously stirred and vented with inert gas (argon). As-prepared FTO suspensions with aimed 1 and 10 mol % fluorine-doping were colloidally stable for months. They exhibit a transparent appearance and a slight bluish shade. As a reference, nondoped SnO_2 (TO) was synthesized similarly. Here, the resulting suspension is again transparent, but colorless.

After the microwave-assisted polyol-synthesis, the resulting suspensions were separated by centrifugation. The slightly bluish powders were redispersed in DEG or ethanol to solid contents of 1 wt % as well as 10 wt %.

Thermal Treatment and Conductivity Measurements. To obtain powder materials, we redispersed the centrifuged sediments in ethanol and centrifuged once more. This washing procedure was repeated three times. Drying was carried out overnight at 70 °C in air. The resulting FTO powders were obtained in quantities of 80−90%. These as-prepared powders (FTO-ap) were then thermally treated: (i) 2 h in air at 500 and 800 °C (FTO-ox); (ii) 2 h in air at 500 °C followed by 2 h in forming gas (H_2/N_2 = 5/95%) at 250 °C (FTO-red). In order to reduce the influence of grain boundaries when evaluating the electrical resistance, powder samples were prepared by pressing to pellets with an IR pressing tool for 15 min at 50 kN (Specac stainless steel pressing tool, 13 mm in diameter; Specac hydraulic laboratory press). The thickness of these pellets was calculated based on materials weight and density (5.6 g cm^{-3}),[31] assuming a space filling of 74% with close-packed nanoparticles.

Basic Characterization. Dynamic light scattering (DLS) of DEG suspensions was measured in polystyrene cuvettes with a Nanosizer ZS from Malvern Instruments. Measurements were conducted of suspensions diluted enough to avoid particle-to-particle interactions, which was determined through a dilution series. Measurements of suspensions with a solids content of 10 wt % were also carried out.

Scanning electron microscopy (SEM) was carried out with a Zeiss Supra 40 VP microscope. Diluted suspensions in DEG were deposited on silicon wafers, the solvent was evaporated and the remainder sputtered with Pt. The acceleration voltage and the working distance were 10 kV and 3 mm, respectively. Statistical evaluation of particle size and size distribution was performed based on the software package Scandium 5.0 from Soft Imaging Systems.

Transmission electron microscopy (TEM) was performed with a Philips CM200 FEG/ST microscope at an acceleration voltage of 200 kV. Samples were prepared by ultrasonic nebulization of an ethanolic dispersion on a Cu grid with a holey carbon film.

X-ray powder diffraction (XRD) was carried out with a Stoe STADI-P diffractometer operating with Ge-monochromatized Cu−K_α radiation. Via the Scherrer equation the crystallite size was deduced based on the full-width-at-half-maximum (fwhm) of selected Bragg peaks. Although additional effects such as lattice strain were not considered, the results allow for comparison with and correlation to the particle size as gained from electron microscopy and dynamic light scattering.

Fourier-transformed infrared (FT-IR) spectra were recorded with a Vertex 70 FT-IR spectrometer from Bruker Optics. The transmittance of pellets consisting of 1 mg sample powder and 300 mg KBr was measured in a wavenumber interval of 7000−370 cm^{-1}.

Brunauer−Emmett−Teller (BET) analysis of as-prepared powder samples was carried out with a BELSORP-mini II from BEL, applying N_2 as adsorbate.

Differential thermal analysis/thermogravimetry (DTA/TG) was performed with a NETZSCH STA 409C using α-Al_2O_3 as a crucible material as well as a reference sample. The samples were heated under N_2 flow to 600 °C with a heat rate of 10 K/min.

Quantitative analysis of the fluorine content was carried out by an commercial microanalytical laboratory, Mikroanalytisches Labor Pascher, Remagen, Germany.

The sheet resistivity of pellets and films was measured via four-point probing using a Keithley system (485 Autoranging Picoammeter, 199 System DMM/Scanner, 230 Programmable Voltage Source). The electrodes were placed in a row and a distance of 1.0 mm to each other. To calculate the sheet resistivity, a geometrical correction factor equal to $\pi/\ln 2$ was applied.[32]

^{119}Sn Mössbauer Spectroscopy. A $Ca^{119m}SnO_3$ source was available for the ^{119}Sn Mössbauer spectroscopic investigations. The samples were placed within thin-walled Plexiglas containers at a

thickness corresponding to about 10 mg Sn/cm^2. A palladium foil of 0.05 mm thickness was used to reduce the tin K X-rays concurrently emitted by this source. The measurements were conducted in the usual transmission geometry at 77 K with a total counting time of 24 h.

Solid-State NMR. The solid-state ^{119}Sn and ^{19}F NMR spectra were recorded on a Bruker Avance II-200 spectrometer operating at the frequencies of 74.65 and 188.35 MHz, respectively (magnetic field strength B_0 = 4.7 T). Magic angle sample spinning (MAS) was carried out with a commercial 2.5 mm double resonance MAS probe. Principal axes values of the ^{19}F chemical shift tensor in SnO_2:F (FTO-ap 1.2 mol %) were determined from a least-squares fitting procedure of a simulated spectrum to an experimental slow MAS NMR spectrum as described in ref 33. The experimental spectrum was performed on a Bruker DSX 500 spectrometer at a ^{19}F Larmor frequency of 470.59 MHz (B_0 = 11.74 T) with a commercial 4 mm triple-resonance MAS probe. CSA values are given in Table 4. Saturation combs were applied prior to all experiments. The ^{119}Sn shifts are referenced relative to neat tetramethyltin. The one-dimensional (1D) ^{19}F NMR spectrum was acquired with a 90° pulse length of 2 μs, a recycle delay (τ_{RD}) of 5 s and at a sample spinning frequency of 25 kHz. Similarly, ^{119}Sn MAS NMR spectra were obtained with direct excitation at a sample spinning frequency of 15 kHz with a 90° pulse length of 2.06 μs and a recycle delay of 1 s. Quantitative ^{19}F MAS NMR spectra (Figure 6) required careful subtraction of the probe background signal. The quantification of the Sn content by MAS NMR on the as-made sample SnO_2:F (FTO-ap 1.2 mol %) was carried out following the guidelines in the literature.[34] One-dimensional (1D) ^{119}Sn{^{19}F} spectra based on ramped cross-polarization[35] (CP) with magic angle spinning (CP-MAS) were obtained at a sample spinning frequency of 15 kHz with a recycle delay of 0.5 s. The spin−lattice relaxation time (T_1) measurements were carried out using a saturation recovery pulse sequence.

During the CP-REDOR experiment,[36] rf nutation frequencies ν_{rf} employed to the hard pulses on the ^{19}F and ^{119}Sn channels were set to 100 kHz. All CP-REDOR experiments were performed at a sample spinning speed of 25 kHz. Relaxation delays were adjusted to 0.5 s. A contact time τ_{CP} of 1.0 ms was used for the ^{119}Sn{^{19}F} CP-REDOR experiment. Sixteen transients/FIDs were accumulated for each measurement. The C-REDOR experiments using CX_x^1 symmetries and a Post C-element[37,38] were conducted at sample spinning speeds bigger than 20 kHz. The C-REDOR data were plotted as $\Delta S/S_0$ against the universal dephasing time τ_{uds},[26] which is a pulse sequence independent time-scale defined from the product $|\kappa|\tau$ of the magnitude of the scaling factor κ and the dipolar dephasing time τ. The scaling factor κ for a REDOR sequence[39] in the δ-pulse limit and C-REDOR are 0.367553 and 0.24503. Fitting of the initial part of the CP-REDOR curve and numerical simulations of MAS NMR spectra were carried out using the SIMPSON[40,41] package to take into account finite pulse effects and interferences between cross-polarization and REDOR.

Background Suppressed 1D/2D ^{19}F NMR. Many commercial MAS NMR probes have a significant ^{19}F background signal due to extensive use of fluorine containing polymers in the stator. Here we present a modified 2D EXSY[42] and a 2D sequence with dipolarly mediated exchange derived from the symmetry based pulse sequence $SR6_6^2$ (Figure 8),[43] where background suppression is achieved by replacing the leading 90° pulse with a DEPTH[44] sequence. The DEPTH experiment was originally developed for imaging purposes by selecting voxels exposed to the same pulse nutation frequency ν_{rf}.[45] In solid-state NMR, the voxels within the sample coil are exposed to the highest pulse nutation frequency and can thus be distinguished from the outside-the-coil voxels, for example those in the stator, by selecting the correct coherence transfer pathway. For the 1D DEPTH experiment $90_{270}(-180_0)_n$−FID a cogwheel phase cycle with $(2n + 1)$ steps turns out to be sufficient.[46] With an increasing number of pulses n, the DEPTH sequence becomes more selective at the expense of losing excitation bandwidth. For our probe, n = 4, 180° pulses ensured a sufficient suppression of the ^{19}F background signal.

The background suppressed 2D-experiments are described in Figure 8. For the 2D-DEPTH-EXSY experiment the cogwheel phase cycle[43] Cog36 (23,5,14,13,14,13,14;0) with 36 steps was employed for coherence transfer pathway selection. The background compensated 2D-DEPTH-$SR6_6^2$ homonuclear zero-quantum recoupling experiment needed a 72 step phase cycle Cog72 (49,13,31,40,41,40,41,40;0). The symmetry-based pulse sequence $SR6_6^2$ with the R-element 270_0-90_{180} was used as previously described in detail.[40] All 2D experiments were obtained with rotor-synchronized t_1 increments, rotor-synchronized mixing times τ_m and 2D data acquisition according to the States method.[47] The nutation frequencies of the hard rf pulses were set to 125 kHz, the sample-spinning frequency was 20 kHz.

COMPUTATIONAL DETAILS

Embedded cluster calculations were performed in order to predict NMR properties of nuclei at or near defect sites. To this end the extended embedded ion method (EEIM) approach[29] was used, whose basic feature is the embedding of the quantum cluster (QC)[48] in an exact, self-consistent point charge field that simulates the environment of an ideal crystal in the electrostatic approximation.

As the EEIM was originally developed for purely crystalline compounds, we outline the two-step procedure for the treatment of point defects in crystals within EEIM in the following. It is assumed that the defect sites occur in a low concentration in the crystal. Hence, in a first step, the embedding point charges can be obtained to a good approximation from a charge optimization using an ideal (i.e., nondefective) crystal/QC, where the usual self-consistent procedure of EEIM as described in ref 29 is employed. In a second step, a QC is created that contains the defect site near its center as well as a larger, roughly radial region with the unperturbed atomic sites of the ideal crystal. The QC region must be large enough to allow a structural relaxation of the defect site, while atoms at the QC boundary must not be relaxed because their direct neighborhood to point charges can result in unrealistic structures. The charge q_{QC} of the doped QC cannot be determined exactly. It should be set to a value that allows a closed shell calculation and is close to the expected fragment charge according to the self-consistent charges determined in the first step and the assumed dopant charge. Formal charges can be used for lowly charged dopants, such as F^-, because the EEIM seems to tolerate small charge misfits of the QC, as demonstrated in calculations on $[Na_{14}F_{13}]^{\pm}$ clusters.[29] The reason is probably, that the charge misfit introduced with the dopant can distribute over the total QC, so that the error in the central region responsible for the main contributions to shielding σ is small. Finally, after completion of the partial structure optimization in presence of the embedding charges, a calculation of NMR parameters is performed. The choice of atomic orbital (AO) basis sets in the final step might differ from the AO set used in previous steps.

The Gaussian 03 program[49] was used for the electronic structure calculations (ESCs) and structure optimizations appearing within EEIM. Population analysis and atomic net charges were determined by the NBO 5.0 program.[50] ESCs in the first step (optimization of embedding charges) were performed at DFT level, using the hybrid functional mPW1PW.[51] A locally dense AO basis was defined by setting up three spherical regions around the nuclei of interest. In the inner region the TZVPP (all electron) atomic basis set on Sn[52] and the 6-311G(3df,3pd) bases[53] for O and F were used. In the second region (at intermediate distances) bases were of double-ζ quality (O,F: 6-31G(d,p)) with pseudo potentials for the core electrons of Sn (LANL2DZp). Small basis sets including pseudo potentials were used in the third region (CEP-4G). Tight convergence criteria were chosen, corresponding to maximum deviations in density matrix elements of

1×10^{-8}, in the energy of 1×10^{-8} Hartree, in the forces of 1.5×10^{-5} Hartree/bohr, and in atomic Cartesian displacements of 6×10^{-5} bohr. Quadrature was performed on an ultra fine grid, i.e., a grid of 99 radial shells and 590 angular points per shell on each atom. Only restricted wave functions were allowed. The final calculations of absolute nuclear magnetic shielding tensors σ were obtained with the GIAO formalism[54] using the same model/basis set combination.

Partial structure optimizations were performed in the presence of embedding charges using nonredundant internal coordinates. In order to keep the calculations feasible the basis set quality in the inner region was reduced to double-ζ quality (6-31G(d,p) for O and F) with pseudo potentials (PPs) on Sn atoms (LANL2DZp basis+PP). An embedded $[Sn_{20}O_{40}F]^-$ cluster was used for the calculation of fluorine on an interstitial site, where the initial position of the F-atom was the face center of a SnO_2 unit cell (see the Supporting Information). In the partial optimization the F-atom and the 12 nearest atoms were allowed to move. Details of the cluster are given in the Supporting Information. An embedded $[Sn_7O_{13}F]^{\pm}$ cluster was used for the calculation of fluorine on an oxygen defect site, where the initial position of the F-atom was at the position of the replaced oxygen atom. Only the fluorine position was allowed to move during the partial optimization. All structure optimizations were performed in C_1 symmetry.

RESULTS AND DISCUSSION

Concepts of Synthesis. Liquid-phase preparation of nanoscaled SnO_2:F (FTO) so far has been performed by utilizing sol−gel methods. There resistivities of 0.7−0.8 Ω cm were achieved for powders.[55,56] Moreover, resistivities of 0.1−1 Ω cm have been reported for sol−gel made thin films.[57,58] Unfortunately, data regarding particle size and size distribution in the liquid phase have not been reported. Based on our knowledge on preparing nanoscaled TCO materials via a polyol-mediated synthesis, this method was selected to realize nanoscaled FTO, too.[59,60] The polyol, i.e., a multidendate high-boiling alcohol such as glycerol, ethylene glycol, or diethylene glycol, allows for efficient control of nucleation and growth of nanoparticles.[61,62] Thus, the size of the nanoparticles can be controlled and their agglomeration suppressed. Moreover, crystalline nanoparticles can be gained because of the high boiling point of the polyols.

Here, SnO_2:F (FTO) nanoparticles with different doping levels were prepared in diethylene glycol (DEG) as the polyol. Heating was performed via microwave irradiation, which turned out to be beneficial for optimized particle size and improved materials crystallinity.[56,63] As-prepared FTO (indicated as FTO-ap) suspensions exhibit a slightly bluish appearance (Figure 1). EDX confirms the presence of fluorine in FTO-ap. However, the accuracy of the method is limited for light elements. Therefore, quantitative analysis was performed by wet-chemical analysis and resulted in 0.4 and 1.2 mol % and are therefore indicated as FTO-ap (0.4 mol %) and FTO-ap (1.2 mol %) in the following. Thus, the fluorine content is significantly lower than compared to the concentration introduced in the synthesis (i.e., 1 and 10 mol %). This finding is ascribed to the very high solubility of $N(CH_3)_4F \cdot 4H_2O$ as the fluorine precursor so that major amounts of fluorine remain in solution. Nevertheless, the incorporation of fluorine is valuably evidenced. Note also that such a quantitative analysis of the dopant content is lacking in literature most often.[52−55]

Size, Size Distribution, and Crystallinity. To investigate the particle size and size distribution of FTO-ap, dynamic light scattering (DLS) was involved first. Measurements were conducted with suspensions right after synthesis as well as with redispersed powder samples in DEG and EtOH (Figure 1).

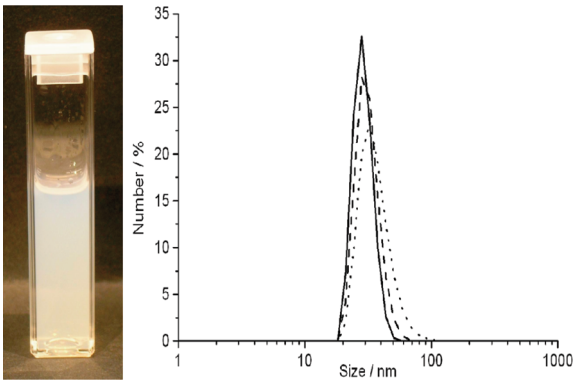

Figure 1. Left, photograph of FTO-ap (0.4 mol %) nanoparticles in a cuvette; right, particle size distribution of FTO-ap (0.4 mol %) in DEG according to DLS analysis: as-prepared suspension (solid), FTO-ap powder redispersed in DEG (dashed), and FTO-ap powder redispersed in EtOH (dotted).

Taking FTO-ap (0.4 mol %) as an example, the size distribution is narrow and similar in all three cases with a mean hydrodynamic diameter around 30 nm (Table 1). The observed facile redispersibility of the nanoparticles is due to a monolayer of DEG that stabilizes the particle surfaces even as a powder sample.[64] For FTO-ap (1.2 mol %), mean particle diameters of 18 nm were obtained (Table 1).

According to scanning electron microscopy (SEM), FTO-ap exhibits a spherical shape with a uniform morphology (Figure 2). Some aggregates of several nanoparticles that are observed on overview-SEM images stem from the drying process when preparing the specimen for electron microscopy. Based on a statistical evaluation of >200 particles, mean diameters of 15(2) nm for FTO-ap (0.4 mol %) and 12(1) nm for FTO-ap (1.2 mol %) were determined (Table 1). SEM images of FTO-ap (0.4, 1.2 mol %) exhibit single crystalline areas of 4(2) nm in size (Figure 2 and the Supporting Information). With 3.3(1) Å, the distance of the lattice fringes agrees well with SnO_2 (cassiterite: (110) with 3.35 Å).[65] These findings indicate that FTO-ap consists of much smaller crystalline domains than one could have assumed from DLS and SEM measurements which indicates that FTO-ap are "polycrystalline" nanoparticles as explained in the introduction.

X-ray powder diffraction confirms the presence of crystalline SnO_2 with the cassiterite-type structure (Figure 3).

On the basis of the Scherrer equation, average monocrystalline domain sizes of 4(2) nm can be deduced (Table 1). In accordance with TEM analysis, this again implies that FTO-ap nanoparticles as observed in suspension (DLS) and powders samples (SEM) exhibit a substructure of much smaller monocrystalline domains. To round-up the investigation of the particle size, nitrogen sorption was performed according to the BET type of method. Specific surfaces of 63(3) $m^2 g^{-1}$ (FTO-ap, 0.4 mol %) and 116(5) $m^2 g^{-1}$ (FTO-ap, 1.2 mol %) were measured. Assuming the presence of spherical and nonporous particles with a bulk-density of SnO_2 (6.9(7) g cm^{-3}),[31] the corresponding particle diameter can be roughly estimated to about 20 and 10 nm (Table 1), which is in sufficient agreement with the values stemming from DLS and SEM.

Finally, thermogravimetry (TG) was performed to study the thermal behavior of FTO-ap nanoparticles and to quantify the amount of DEG adhered on the nanoparticle surface. Here, a continuous weight loss up to 12.9(3)% was observed for FTO-ap between 200 and 400 °C. According to previous studies as well as

dx.doi.org/10.1021/cm103286t |Chem. Mater. 2011, 23, 1526–1538

Table 1. Overview of Thermal Treatment and Analytical Characterization of FTO Samples

type of sample	particle size (nm) (DLS)[a]	particle size (nm) (SEM)[b]	crystallite size (nm) (XRD)[c]	BET surface $(m)^2\ g^{-1}$
FTO-ap (0.4 mol %) air, 70 °C, 8 h	29(2)	15(2) (primary particles)	4(2)	63(3)
FTO-ox-500 (0.4 mol %) air, 500 °C, 2 h		51(4) (agglomerates)	11(2)	34(2)
FTO-red (0.4 mol %) 1. air, 500 °C, 2 h 2. N_2/H_2, 250 °C, 1 h		59(4) (agglomerates)	11(2)	35(2)
FTO-ox-800 (0.4 mol %) air, 800 °C, 0.5 h		64(4) (agglomerates)	21(3)	12(2)
FTO-ap (1.2 mol %)air, 70 °C, 8 h	18(2)	12(1) (primary particles)	4(2)	116(5)
FTO-ox-500 (1.2 mol %) air, 500 °C, 2 h		85(5) (agglomerates)	10(2)	41(3)
FTO-red (1.2 mol %) 1. air, 500 °C, 2 h 2. N_2/H_2, 250 °C, 1 h		87(5) (agglomerates)	10(2)	39(3)
FTO-ox-800 (1.2 mol %) air, 800 °C, 0.5 h		85(5) (agglomerates)	19(3)	15(2)

[a] Deduced from DLS analysis of suspensions in DEG. [b] Deduced from SEM images by statistical evaluation of a manifold of >200 particles as given in brackets. [c] Deduced from XRD via the Scherrer equation.

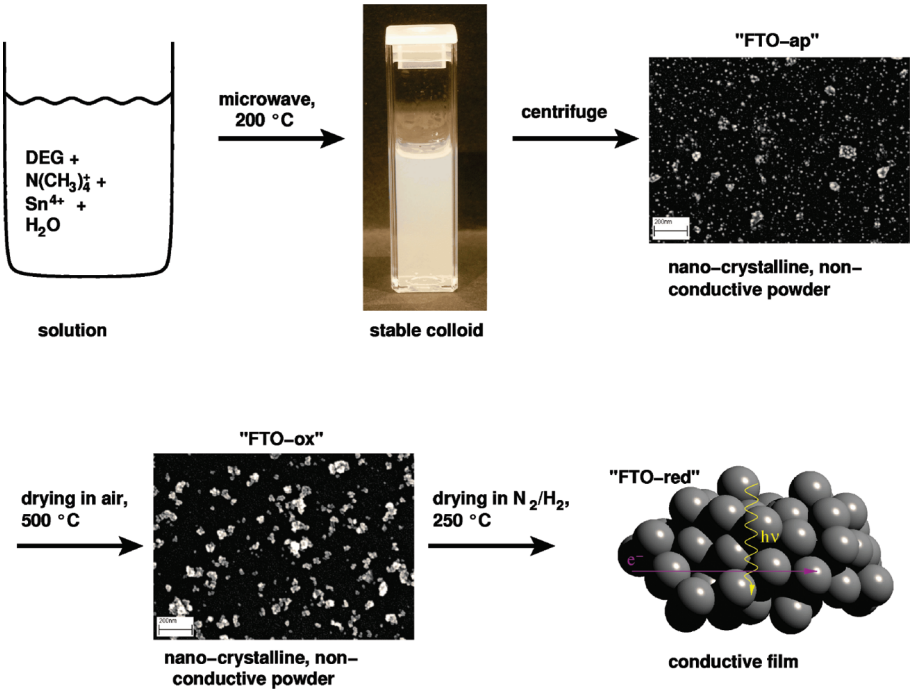

Figure 2. Simplified flow-diagram showing synthesis, products, and main properties.

the boiling point of DEG (248 °C),[31] this weight loss can be related to DEG adhered on the particle surface.[36,66] This finding is in agreement with the excellent redispersibility of FTO-ap powder samples in DEG and ethanol.

Electrical Conductivity and Thermal Treatment. To investigate the conductivity of FTO-ap, powder samples were first pressed to pellets. This measure guarantees a close contact between the individual nanoparticles. Thereafter, the pellets were investigated by four-point probing. Accordingly, FTO-ap samples did not show any measurable conductivity. Aiming at conductive materials, FTO-ap was thermally treated in order to, first, remove residual DEG and water, and second, diminish grain boundaries between different monocrystalline domains. With regard to TG analysis, as-prepared FTO was therefore annealed under oxidizing conditions in air at 500 °C for 2 h. To differentiate from as-prepared FTO (FTO-ap), these samples heated in air were indicated as FTO-ox-500 in the following (Table 1). The FTO samples were reductively processed in forming gas at 250 °C for 1 h to establish free charge carriers subsequent to the first oxidative thermal treatment,(FTO-red). Both of these thermal treatments, the oxidative as well as the reductive one are quite typical and often applied to process transparent conductive oxides.[4,10] To study for further structural and morphological effects, the FTO samples were finally heated in air at 800 °C for 30 min (indicated as FTO-ox-800, Table 1).

In the following FTO-ox and FTO-red were similarly characterized regarding particle size and crystallinity as discussed for FTO-ap. According to X-ray powder diffraction, the post-treated samples consist of phase pure cassiterite type SnO_2. The monocrystalline domain size was again calculated via Scherrer's formula and lead to 11 nm for FTO-ox as well as FTO-red (Table 1). As expected, processing in forming gas at 250 °C has no effect on the monocrystalline domain size. On the other hand, samples treated at even higher temperatures (FTO-ox-800) exhibit monocrystalline domain sizes of 19(3) nm implying a solid-state Oswald ripening process (Table 1). Subsequent to annealing at 500 and 250 °C, SEM images of FTO-ox and FTO-red show polycrystalline nanoparticles of 50−80 nm in diameter (Figure 2). These particles consist of several smaller primary particles (FTO-ap) (Table 1) giving evidence of an

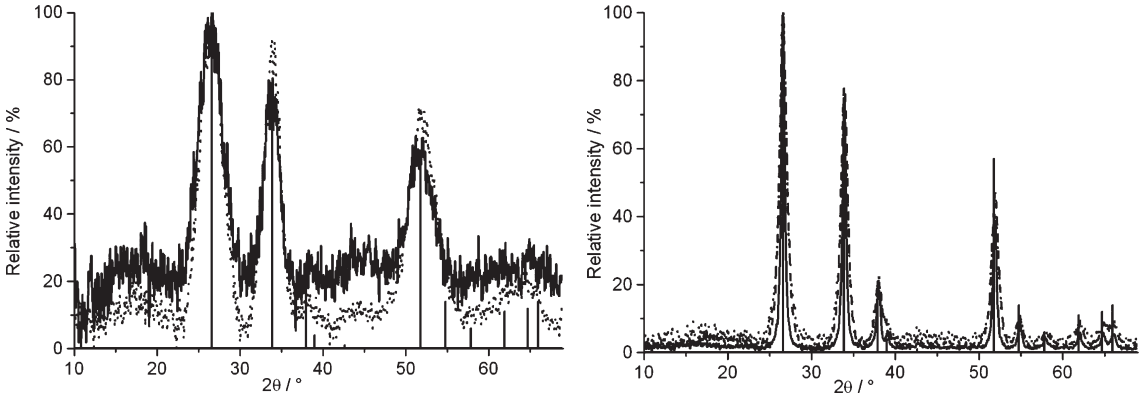

Figure 3. X-ray diffraction patterns (Cu radiation) of FTO nanoparticles; left: FTO-ap (0.4 mol %) (solid), FTO-ap (1.2 mol %) (dotted), right: FTO-ox-500 (dashed), FTO-red (dotted), FTO-ox-800 (solid) (reference: SnO_2, ICDD No. 41−1445) (vertical lines).

agglomeration process. Partly, even individual nonagglomerated primary particles of this size are still visible. If the FTO nanoparticles are treated at even higher temperatures (FTO-ox-800) the substructure of the agglomerates disappears so that compact aggregates remain. BET analysis of the specific surface confirms the findings and trends from XRD and SEM (Table 1).

XRD, SEM and BET validate that even the agglomerated FTO samples obtained after the oxidative and reductive heat treatment are still nanoscaled and with diameters below 100 nm. With this knowledge, four-point probing was performed. To establish close contacts between the nanoparticles, FTO-red (0.4 and 1.2 mol %) as well as nondoped SnO_2 powders treated with forming gas (TO-red) were pressed to pellets prior to the electrical characterization. The resulting sheet resistances and specific resistivities are compiled in Table 2.

As expected, even nondoped SnO_2 (TO-red) shows a remarkable conduction due to oxygen vacancies. Fluorine doping nevertheless results in a significantly reduced resistivity with 13 and 0.2 Ωcm as the lowest values in the case of FTO-red (1.2 mol %). Comparing these values to literature, the resistivity of the FTO-red (0.4 mol %) is similar to what was reported on powders gained via the sol−gel method.[52,53] The resistivity of FTO-red (1.2 mol %) is even lower and matches sol−gel films prepared by Biswas et al.[57] Thus, the polyol method gives an easy access to conductive FTO samples without the need of advanced metal−organic precursors as required for the sol−gel synthesis.[52−55]

Structural Models. How is fluorine incorporated into the structure of the polycrystalline SnO_2 nanoparticles? For SnO_2:F deposited in thin layers several structural models are currently discussed[2] that are consistent with Hall effect measurements which give evidence of n-doping. Several point defects can be considered to explain n-doping of SnO_2:F. Provided that charge neutrality is maintained in the particles, only defects representing a positive charge relative to the host structure SnO_2 can introduce excess electrons. The defects are conveniently written in Kröger−Vink notation[67] as follows:

(i) oxygen vacancies $V_O^{\bullet\bullet}$ (+ $2e^-$ delocalized)
(ii) fluorine filled oxygen vacancies $F_O^{\bullet}$ (+ e^- delocalized)
(iii) tin on interstitial sites $Sn_i^{\bullet\bullet\bullet\bullet}$ (+ $4\,e^-$ delocalized)
(iv) hydrogen on interstitial sites $H_i^{\bullet}$ (+ e^- delocalized)

Oxygen vacancies are related to oxygen vapor pressure $p(O_2)$ and are generated in pure SnO_2 at higher temperatures[36,68] according to the following defect equilibrium

$$O_O \rightleftarrows 1/2O_2 \uparrow + V_O^{\bullet\bullet} + 2e'$$

Table 2. Sheet Resistance and Resistivity of Post-Treated Doped and Nondoped Tin Oxide Samples According to Four-Point Probing Measurements

type of sample	sheet resistance (Ω/sq)	resistivity (Ω cm)
TO-red	700(10)	14.0(2)
FTO-red (0.4 mol %)	60(4)	0.9(4)
FTO-red (1.2 mol %)	13(2)	0.2(1)

For nanoparticles, the situation is complicated by the high surface area which is likely to host a variety of chemical environments of tin, oxygen and fluorine. Also for nanoparticles the charge neutrality criterion applies. However, electrons introduced by doping with different defects may prefer to be localized at the surface rather than increasing the charge carrier concentration in the particle core. A particle core of the composition $Sn(IV)O_{2-x}$ doped with x F should carry a positive charge, which would have to be balanced by a negative charge at the particle surface. This process would also limit the size of the nanoparticles and stabilize the colloids. Because of its band structure, SnO_2 is able to convey charge from core to shell, which is underlined by the DFT calculations presented below (electron difference plot, Figure 14, right-hand side). Clearly, it is essential to the electrical conductivity to treat the nanoparticles with a reducing agent after precipitation, i.e., here the forming gas, in order to finally provide the electrons for n-doping.

How is structure related to electrical resistivity?

Several factors contribute to the observed bulk resistivity. Important are the charge carrier concentration, grain boundary scattering, lattice vibrations and ionized impurity scattering.[36] An optimum conductivity exists because the charge carrier concentration will decrease resistivity and the scattering at ionic defects will increase resistivity with increasing F doping. Literature values obtained on SnO_2:F films indicate that ideal behavior is reached around 6−8 wt % for fluorine doping.[69,70] Next to doping also treatment with different gases may influence the charge carrier concentration. In our case, treatment of the nanoparticles with forming gas at elevated temperatures will increase the number of oxygen vacancies.[71]

The nanoscale structure of the prepared SnO_2:F adds further factors which influence electrical resistivity. The charge carrier concentration may be lower than expected because electrons introduced by doping are localized at the surface of the nanoparticles[2] and not, as intended, delocalized in the SnO_2

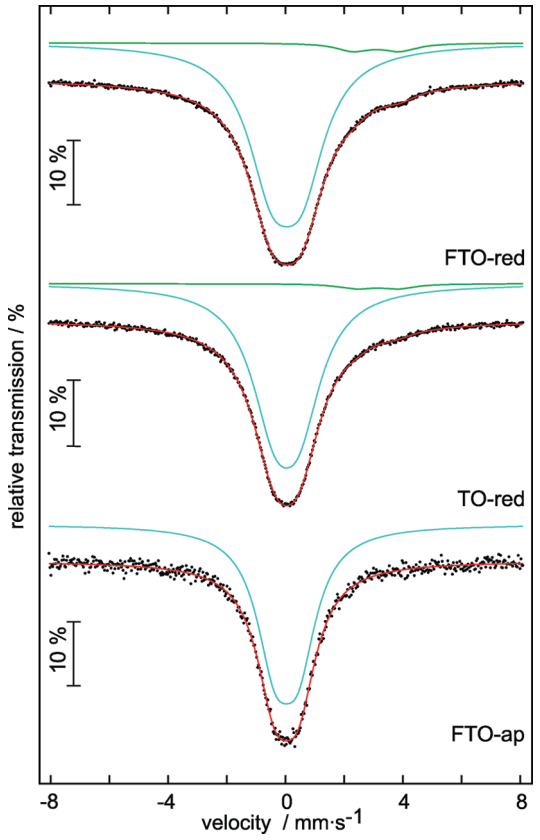

Figure 4. Experimental and simulated ^{119}Sn Mössbauer spectra of tin-oxide nanoparticles: FTO-red 1.2 mol %, nondoped SnO_2-nanoparticles treated with forming gas (TO-red), and FTO-ap 1.2 mol % measured at 77 K.

conduction band.[72] Furthermore, the grain boundaries between different nanoparticles will contribute to resistivity.

The purpose of the magnetic resonance techniques below is to shade some light onto the role of fluorine doping in this case. Important issues are to find out if F atoms prefer the shell or are rather homogeneously doped into the SnO_2 particles and in which environments/site F atoms are located.

^{119}Sn Mössbauer Spectroscopy. A ^{119}Sn Mössbauer spectrum of a SnO_2:F sample after treatment with forming gas (FTO-red) recorded at 77 K is presented at the top in Figure 4 together with transmission integral fits.

The spectrum is composed of one main component at an isomer shift of $\delta = 0.04(2)$ mm/s and an experimental line width of $\Gamma = 1.97(8)$ mm/s, subject to quadrupole splitting of $\Delta E_Q = 1.01(4)$ mm/s. This signal contributes 95.6(2)% to the total intensity of the Mössbauer spectrum. The shoulder at higher velocity accounts for the second signal at an area of 4.4(2)%. The latter signal has an isomer shift of $\delta = 3.09(2)$ mm/s, and an experimental line width of 1.36(7) mm/s and a quadrupole splitting parameter of $\Delta E_Q = 1.58(3)$ mm/s. The fitting parameters are summarized in Table 3.

The main contribution can certainly be ascribed to tetravalent tin of SnO_2, cassiterite, which itself has an isomer shift close to zero,[27,73] similar to the stannate source used for the experiment. The slightly increased line width along with the quadrupole splitting parameter can be ascribed to the O/F disorder in the local Sn(IV) environment and/or disorder associated to the nanoscale character of these particles. The isomer shift of the second spectroscopic contribution ($\delta = 3.09(2)$ mm/s) does not agree with the isomer shift of divalent tin fluoride SnF_2 ($\delta \approx 3.5$ mm/s)[74,75] and SnO (2.7 mm/s).[27,70] Note that the electron density in the s- and p-valence-orbitals at the Sn atom determines the isomer shift.[27,76] The electrons contributed by doping would contribute to a small change in shift of the Sn(IV) resonance if they were delocalized in the SnO_2 conduction band as it has been observed for SnO_2:In[77] or SnO_2:Sb.[78] Thus the ^{119}Sn isomer shift probes the electron concentration in the conduction band. The observed isomer shifts indicate that the electrons contributed by forming gas and F-doping do not behave as expected for a bulk material but the extra electrons are localized at specific tin atoms or defects which is strongly indicated by the observation of the second resonance at ($\delta = 3.09(2)$ mm/s) typical for Sn(II).

By treating the as-made sample with forming gas at elevated temperatures the surface may partially be reduced and further O-defects are induced into the SnO_2 host. For this reason, we have also measured two reference samples (Figure 4 and Table 3), non doped SnO_2 nanoparticles reduced with forming gas (TO-red), and FTO-ap. The fitting parameters (Table 3) for sample TO-red are comparable to FTO-red. In contrast to samples TO-red and FTO-red, the ^{119}Sn spectrum shows exclusively tetravalent tin for FTO-ap (estimated Sn(II) detection limit: 0.5%). We conclude that at the current level of F-doping the biggest effect in terms of conduction electron concentration is related to the treatment with forming gas. Finally, we need to consider that the Mössbauer f-factors for the Sn(II) and Sn(IV) signals differ at 77 K, underestimating the Sn(II) contribution.[79] Also the crystallite size plays an important role, similar to crystalline and amorphous pure SnO_2.[80]

Solid-State NMR spectroscopy. By solid-state NMR, the SnO_2 host, the nanoparticle interfaces, and the environments of the doped F-atoms can be studied. In the following we start first with the findings from 1D experiments (^{119}Sn, ^{19}F). Then we probe the homogeneity of F-doping with homonuclear recoupling experiments and finally we determine constraints for F−Sn or H−F distances by REDOR experiments.

^{119}Sn and ^{19}F 1D MAS, Direct Excitation. The ^{119}Sn MAS NMR spectrum of bulk SnO_2[81] shows one sharp resonance at −604.7 ppm (Figure 5, top) in accordance with the cassiterite structure, i.e. one Sn site per unit cell and Sn(IV) in almost regular octahedral surrounding. NMR is able to distinguish Sn(II) from Sn(IV),[82] similar as Mössbauer spectroscopy can do; however, small amounts of Sn(II) are difficult to detect because of a much bigger dispersion of the chemical shift values and an order of magnitude bigger chemical shift anisotropies than for Sn(IV) environments.

For as-made SnO_2:F nanoparticles (FTO-ap 1.2 mol %), a single broad resonance is observed at −604.6 ppm (Figure 5 and Table 4). Its line width of 23.2 ppm is typical for nanoparticles[83] and is related to doping induced disorder, particle size, and surface/interface effects.

A critical question for the NMR study is if the NMR spectra are representative for all nuclei in the sample or if part of them are unobservable, for example by effective spin−lattice relaxation or an extreme Knight shift. To answer this question we have recorded a quantitative ^{119}Sn spectrum of a well-defined mixture of bulk crystalline SnO_2 and of as-made SnO_2:F nanoparticles, and we have compared the peak area ratios to the expected value. The mass of the nanoparticles was corrected for water and DEG being attached to the particle surface. The correction factor was obtained from a thermogravimetry trace up to a temperature of

Table 3. Fitting Parameters for ^{119}Sn Mössbauer Spectra of Samples FTO-red 1.2 mol %, Nondoped SnO_2 Nanoparticles Treated with Forming Gas (TO-red), and FTO-ap 1.2 mol % Measured at 77 K[a]

sample	δ_1 (mm s^{-1})	ΔE_{Q1} (mm s^{-1})	Γ_1 (mm s^{-1})	δ_2 (mm s^{-1})	ΔE_{Q2} (mm s^{-1})	Γ_2 (mm s^{-1})	Area 1:2 (%)
FTO-red	0.04(1)	1.01(1)	1.97(1)	3.09(2)	1.58(3)	1.36(7)	96:4
TO-red	0.04(1)	0.84(1)	1.91(1)	3.08(1)	1.44(4)	1.36*	97:3
FTO-ap	0.03(1)	0.79(1)	1.52(1)				

[a] δ, isomer shift; ΔE_Q, electric quadrupole splitting parameter; Γ, experimental linewidth; parameters marked with an asterisk were kept fixed during the fitting procedure.

900 °C. The agreement of observed ratio and expected ratio, 3.96 and 3.94, respectively, is well within the error limits, which indicates that solid-state NMR spectra under the chosen conditions are representative for all NMR active nuclei in the sample.

^{19}F MAS NMR allows to study the environments of the F atoms doped into the SnO_2 nanoparticles. Background corrected ^{19}F MAS NMR gives evidence of a single, relatively broad resonance at −113.9 ppm, shown in Figure 6.

This value may be compared to the isotropic chemical shift values of crystalline SnF_2 (−110.4 ppm)[28] or SnF_4 (−146.9 ppm).[84] The literature values indicate that the chemical shift of ^{19}F is a sensitive probe of its electronic environment, indicating that only a single type of environment is present in SnO_2:F nanoparticles. Its chemical shift anisotropy was determined at a higher magnetic field of 11.74 T. An assignment to the different defect models (Figure 14) will be made below on the basis of quantum chemical calculations and ^{119}Sn{^{19}F} CP-REDOR experiments.

In a series of quantitative ^{19}F NMR experiments we packed the NMR rotor with similar amounts of sample which was taken from the same batch but dried in air at different temperatures (Figure 7). While the electrical properties of these samples and their colors hardly change, there is a significant decrease of the ^{19}F signal, which gives evidence of fluorine leaving the sample before the sample is treated with the forming gas and before it shows an increase in electrical conductivity. We conclude that F-doping of SnO_2:F nanoparticles is not directly related to an increase of the charge carrier concentration but instead it may help to reduce grain-boundary scattering in electron transport upon leaving the sample at higher temperatures.

2D ^{19}F homonuclear correlation spectroscopy. Apart from the chemical shift solid-state NMR offers the magnetic dipole−dipole coupling to study the proximity of NMR active nuclei. The through-space dipolar coupling between pairs of ^{19}F atoms can thus be used to check whether fluorine is homogeneously doped into the sample or whether fluorine atoms "cluster" around specific Sn atoms. For this purpose, background compensated 2D-DEPTH-SR6$_6^2$ (pulse-sequence: Figure 8B) experiments were conducted on the sample FTO-ap (1.2 mol %).

In the resulting correlation spectra (Figure 9, right-hand side) off-diagonal peaks are expected when two fluorine atoms are attached to the same Sn-atom, i.e. if they are at distance of less than 420 pm. Since all the signal intensity, even at long mixing times (1.8 ms), is found on the diagonal, we can conclude that no more than one F atom is attached to a single Sn atom. Several attempts with different double-quantum filtered experiments[85,86] have accordingly not been successful (results not shown).

To cross check this conclusion we have performed background-compensated 2D-DEPTH-EXSY experiments which apart from eventual F motion can be used to evaluate the inhomogeneous line width of the diagonal peaks in the previous experiment. Since the diagonal peaks in both 2D spectra in Figure 9 essentially have the same width, we have no indication of dipolar contacts in the 2D-DEPTH-SR6$_6^2$ experiment between F atoms of similar chemical shift values. Moreover, 2D-DEPTH-EXSY gives no evidence of F motion at a time scale of 0.256 ms at room temperature, which admittedly is rather unlikely from a chemical point of view.

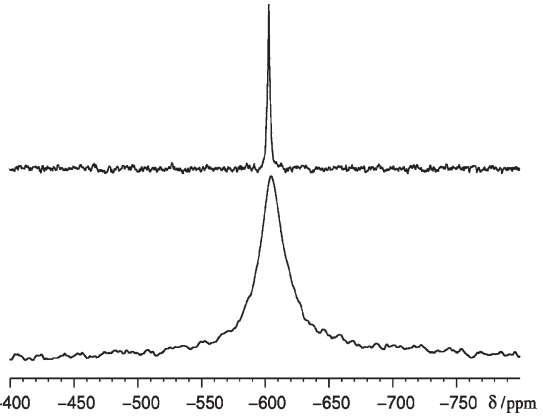

Figure 5. ^{119}Sn MAS NMR spectra of bulk polycrystalline SnO_2 (top) and SnO_2:F (FTO-ap 1.2 mol %, bottom), obtained at a sample spinning frequency of 15 kHz.

^{119}Sn{^{19}F} CP MAS NMR. To characterize the F environment in more detail ^{119}Sn{^{19}F} cross-polarization (CP) experiments were performed.

At short contact times Sn atoms closest to F will dominate the spectrum in terms of intensity (Figure 10, top), here peak B at δ_{iso}=−635.8 ppm. As expected for F atoms doped into the SnO_2 host structure, peak A at δ_{iso}= −604.6 ppm appears at long contact times in agreement with the chemical shift of the main resonance of the direct excitation ^{119}Sn MAS spectrum (Figure 5).

^{119}Sn{^{19}F} CP-REDOR NMR. Because cross-polarization experiments allow us to access both Sn and F at the defect site, we used the ^{119}Sn{^{19}F} CP-REDOR experiment[35] to estimate the distance between F and Sn. Both ^{19}F and ^{119}Sn can be treated as diluted spin-systems: ^{19}F because of homogeneous doping, ^{119}Sn because the natural abundance is only 8.6%. The experimental CP-REDOR curve can then be simulated in a two-spin approximation (Figure 11).

The simulation was performed taking both the CP-REDOR experiment and the effect of the cross-polarization experiment into account. The fit of the initial regime ($\Delta S/S_0 < 0.2$, $\Delta S = S_0 - S$) led to a magnetic dipole−dipole coupling constant ν_{dip} of 4907 Hz (Figure 11), which amounts to a Sn−F distance of 205 pm. This distance is in accordance with the Sn−O bond distance of 205.2 pm in SnO_2.[87] Thus it can be concluded that the

Table 4. ^{119}Sn and ^{19}F Chemical Shift Parameters and Spin−Lattice Relaxation Times of Fluorine-Doped Tin Oxide (FTO-ap 1.2 mol %)[a]

compound/ [cluster]	isotope	signal	δ_{iso} (ppm)	δ_{aniso} (ppm)	η	δ_{11}(ppm)	δ_{22}(ppm)	δ_{33} (ppm)	T_1 (s)
bulk SnO_2 (cassiterite)	^{119}Sn	exp.	−604.7						2.8
SnO_2:F (FTO-ap 1.2 mol %)	^{119}Sn	exp. peak A	−604.6						29.1
	^{119}Sn	exp. peak B	−635.8(5)						
SnO_2:F (FTO-ap 1.2 mol %)	^{19}F	exp.	−113.9	−81	0.64	−47.4	−99.3	−195.0	0.17
$[Sn_7O_{13}F]^+$ $F_O^\bullet$ (defect)	^{19}F	calc.[b]	−108(12)	72(23)	0.5(4)	−35	−126	−161	
$[Sn_7O_{13}F]^-$ F_O' (defect)	^{19}F	calc.[b]	−121(12)	67(23)	0.6(5)	−53	−136	−174	
$[Sn_{20}O_{40}F]^-$ F_i' (interstitial)	^{19}F	calc.[b]	+82(12)	−218(23)	0.1(1)	201	180	−136	

[a] δ_{11}, δ_{22}, and δ_{33} are the principal axis values; definitions of the δ_{iso}, δ_{aniso}, and η are the same as in SIMPSON,[37,38] which was used to fit the experimental data; the estimated error for the calculated principal axis values of ^{19}F is in the range 20 ppm; the error estimates for δ_{iso},δ_{aniso}, and η stem from error propagation. [b] Shift calculated by the conversion equation δ = 191.46 ppm−1.046σ obtained from calibration on 43 experimental and calculated ^{19}F shift values with the mPW1PW/6-311G(3df,3pd) model (see the Supporting Information).

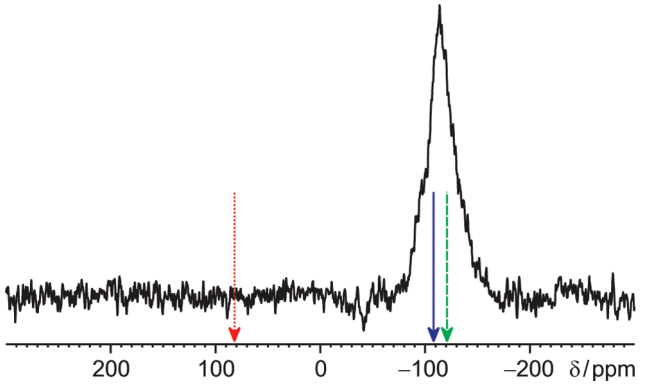

Figure 6. ^{19}F spin echo MAS NMR spectrum of SnO_2:F (FTO-ap 1.2 mol %) at a sample spinning frequency of 25 kHz; arrows indicate the calculated chemical shifts for various clusters; red arrow at 82 ppm: $Sn_{20}O_{40}F$ (F_i' interstitial site); blue arrow at −108 ppm: $[Sn_7O_{13}F]^+$ ($F_O^\bullet$ defect site); green arrow at −121 ppm: $[Sn_7O_{13}F]^-$ (F_O' defect site).

^{119}Sn{^{19}F} CP-REDOR experiment is in agreement with a fluorine filled oxygen vacancy.

^{19}F{^{1}H} C-REDOR, ^{119}Sn{^{1}H} C-REDOR NMR. In Table 1 particle sizes from various techniques are collected. They indicate that FTO-ap (1.2 mol %) has a mean diameter of about 15 nm while that of monocrystalline domains is only 4 nm. A single nanoparticle has therefore many inner grain-boundaries which contribute to electrical resistance. The question arises whether the interface between two different lattice planes can host different atoms. Under the assumption of a homogeneously F-doped material ^{19}F{^{1}H}-C-REDOR can be used to investigate if hydrogen atoms are located at these inner interfaces, by measuring the magnetic dipole−dipole coupling of ^{1}H at the surface and ^{19}F or ^{119}Sn atoms in the particle core. We have predicted ^{119}Sn{^{1}H}-C-REDOR curves for spherical nanoparticles of different sizes (Figure 12) under the assumption of a constant surface occupancy A of 1.5 · 10^{19} H atoms/m^2 which has been estimated from the cassiterite crystal structure for spherical particles of 2−5 nm, which are saturated by oxygen at the surface and neutral in charge (see the Supporting Information). Furthermore we assume that the individual superimposed REDOR curves can be treated in a 2-spin approximation which strictly speaking is only correct for the initial regime of the REDOR curve (see ref 26 for details of the effective dipolar coupling and the superposition integral).

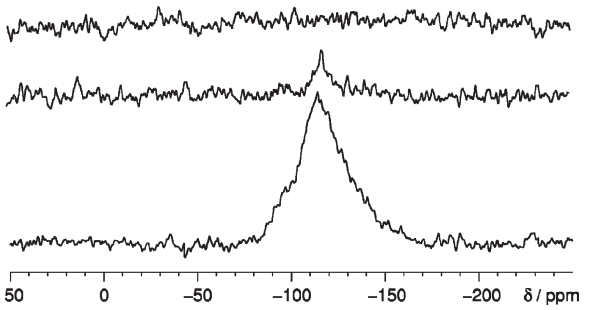

Figure 7. Quantitative background corrected ^{19}F MAS NMR spectra of as-made fluorine doped tin oxide (FTO-ap 1.2 mol %, bottom); fluorine doped tin oxide heated to 500 °C (FTO-ox-500 1.2 mol %, middle) and to 800 °C (FTO-ox-800, top) with direct excitation at a sample spinning frequency of 25 kHz; approximately the same amount of sample was packed into the rotors and similar experimental conditions were applied.

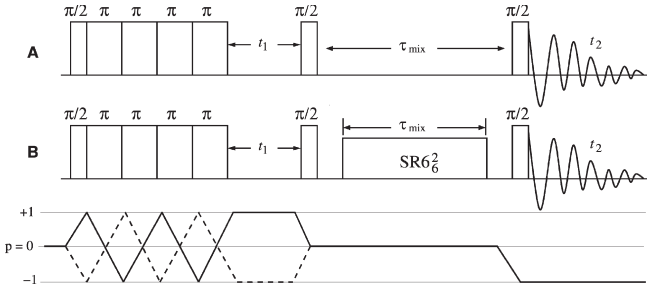

Figure 8. Background suppressed 2D experiments: (A) 2D-DEPTH4-EXSY and (B) 2D-DEPTH-SR6$_6^2$; the coherence transfer pathway diagram below indicates which pathways were selected to obtain pure absorption 2D spectra.

Then closed analytical functions for the effective dipolar coupling constant ν_{eff} can be derived by integration over the magnetic dipole−dipole coupling from a single ^{119}Sn atom in the particle core to all ^{1}H atoms at the particle surface, which depends on the radius of the nanoparticle r_{pa}, the distance of the observed ^{119}Sn atom to the particle center r_{ob}, the gyromagnetic ratios $\gamma_{^{19}F}$, $\gamma_{^{119}Sn}$ and the surface occupancy A.

$$\nu_{eff} = \frac{|\gamma_{^{19}F}\gamma_{^{119}Sn}|\mu_0\hbar}{4\pi\sqrt{\pi}} \frac{r_{pa}\sqrt{A(r_{pa}^2 + r_{ob}^2)}}{(r_{pa}^2 - r_{ob}^2)^2}$$

dx.doi.org/10.1021/cm103286t |*Chem. Mater.* 2011, 23, 1526–1538

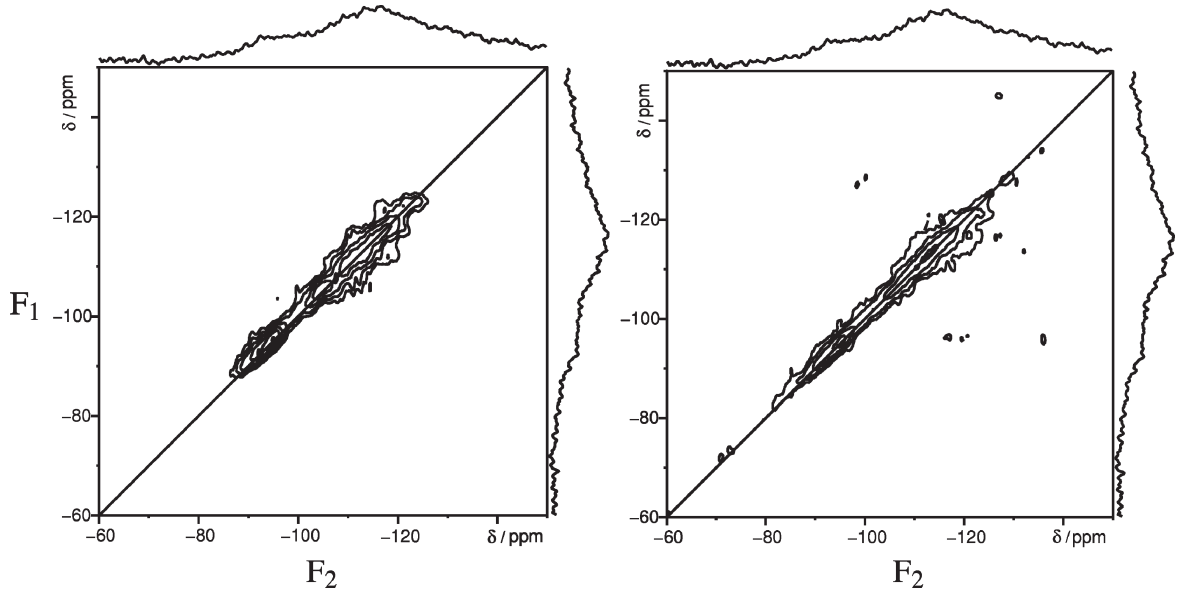

Figure 9. ^{19}F 2D-DEPTH-EXSY spectrum (left) and background-compensated zero-quantum 2D homonuclear-correlation ^{19}F spectrum (right) of SnO_2:F (FTO-ap 1.2 mol %), at a sample spinning frequency of 25 kHz; the $SR6_6^2$ pulse sequence was used to generate a zero-quantum Hamiltonian (Figure 8); the mixing interval for background compensated 2D-$SR6_6^2$ and 2D-exchange were τ_{mix} = 1.8 ms and τ_{mix} = 0.256 ms, respectively; apart from noise, no off-diagonal peaks are visible.

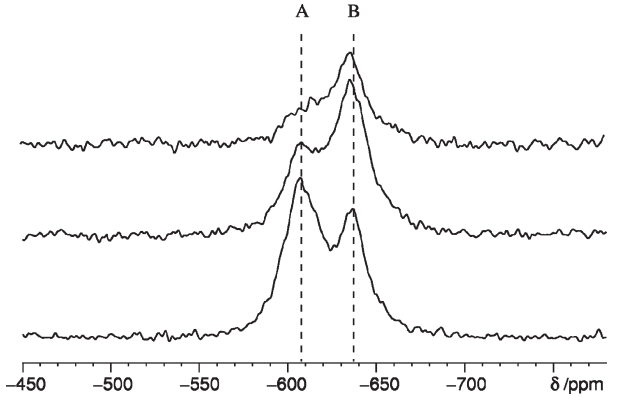

Figure 10. ^{119}Sn{^{19}F} CP-MAS NMR spectra of fluorine doped tin oxide, SnO_2:F (FTO-ap 1.2 mol %) recorded with different contact times (from bottom to top): 5.0, 1.0, and 0.5 ms; each spectrum obtained with 0.5 s recycle delay, at a sample spinning frequency of 15 kHz.

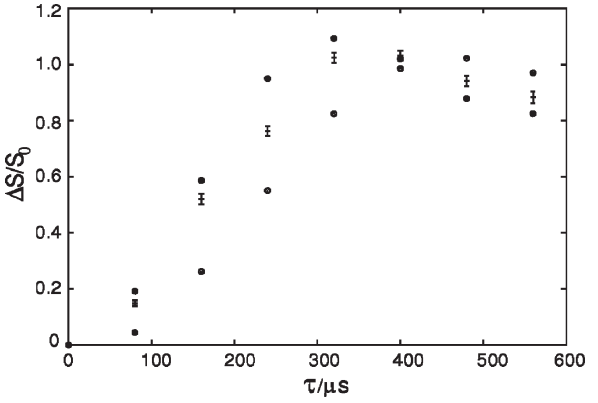

Figure 11. ^{119}Sn{^{19}F} NMR CP-REDOR curve of fluorine doped tin oxide (FTO-ap 1.2 mol %); points with error bars denote experimental data points obtained at a sample spinning frequency of 25 kHz and a contact time of 1 ms; data denoted by filled and empty circles were obtained by numerical simulation for a 2 spin-system with magnetic dipole−dipole coupling constants of 4907 and 3767 Hz for defect and interstitial sites (Figure 14), respectively (see text).

From the comparison of simulated ^{119}Sn{^{1}H} REDOR curves with experimental curves, we conclude that the interfaces of the monocrystalline regions are saturated with ^{1}H atoms (Figure 12) because the particle diameter of 2 nm of the simulated best fit is on the same order as the values obtained by X-ray diffraction.

In principle, ^{119}Sn{^{1}H} and ^{19}F{^{1}H} REDOR curves are redundant if ^{19}F is homogeneously doped into the SnO_2 particle. When the dephasing times τ of both curves are multiplied by the gyromagnetic ratios of $\gamma_{^{119}Sn}$ and $\gamma_{^{19}F}$, respectively, they should exactly overlap if ^{19}F is perfectly homogeneous. Experimental data (Figure 13), however, show a significantly faster dephasing behavior for ^{19}F than for ^{119}Sn, which proves that F atoms prefer sites closer to the intraparticle surfaces, which means that ^{1}H−^{19}F distances are shorter than the corresponding ^{1}H−^{119}Sn counterparts.

Quantum Chemical Calculations. The previous experimental investigations indicate that F atoms are incorporated into the SnO_2 host structure. In the following we study two different models, i) fluorine occupies O vacancies and ii) fluorine occupies interstitial sites, by quantum chemical calculations and compare the predicted chemical shift values to the experimental ones. Moreover, the shortest internuclear F−Sn distances can be predicted.

The approximate locations of the two sites in a crystalline SnO_2 environment are visualized in Figure 14. The biggest cavity for a potential interstitial site is located near the face-centers of the SnO_2 unit cell (see the Supporting Information). Placing a fluorine ion exactly at the position of an oxygen site seems to be a reasonable, first approximation to an oxygen replacement site. It

dx.doi.org/10.1021/cm103286t |*Chem. Mater.* 2011, 23, 1526–1538

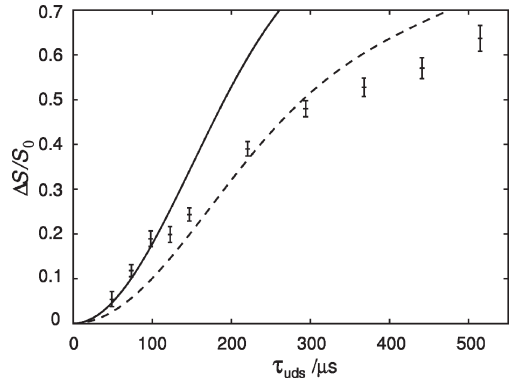

Figure 12. $^{119}Sn\{^1H\}$ NMR C-REDOR curve, ^{119}Sn observed; points with error bars denote experimental data obtained at a sample spinning frequency of 20 kHz; solid and dashed lines were obtained by numerical simulation for spherical nanoparticles in a 2-spin approximation valid only for the initial regime ($\Delta S/S_0 < 0.2$) of the REDOR curve with particle diameters of 2.0 and 3.0 nm, respectively (see text).

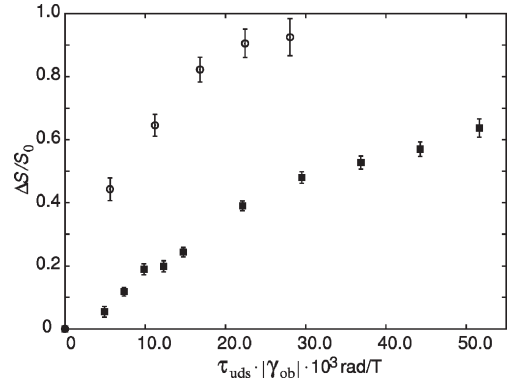

Figure 13. $^{19}F\{^1H\}$ C-REDOR (circles) and $^{119}Sn\{^1H\}$ C-REDOR (squares) curves, ^{19}F and ^{119}Sn observed, respectively; experimental data obtained from a $^{19}F\{^1H\}$ and $^{119}Sn\{^1H\}$ C-REDOR experiment at a sample spinning frequency of 22 and 20 kHz, respectively; the dephasing times τ of both curves are multiplied by the gyromagnetic ratios of γ_{ob}, so that equal $^{19}F-^1H$ and $^{119}Sn-^1H$ distances would lead to overlapping curves in this plot.

is expected that the crystal structure will be perturbed in the vicinity of the dopant. Therefore, we performed separate partial structure optimizations for the two defect sites by EEIM calculations in the presence of a SnO_2 crystal field. For interstitial site doping we created a $[Sn_{20}O_{40}F]^-$ cluster and allowed structural relaxation of the F-atom and the atoms in its next coordination sphere ($r \leq 3.2$ Å). The final optimized structure is shown in Figure 14. Obviously, the F-atom does not fit well into the cavity and hence significant distortions of the surrounding atoms are observed. The F-atom is located on site with a short F−O distance of 1.493 Å and a minimal F−Sn distance of 2.241 Å.

A fluorine doping on an oxygen defect site is simulated by an $[Sn_7O_{13}F]^+$ cluster, where we allowed structural optimization of the fluorine atom only. The final structure is shown in Figure 14 on the right side. The deviation of the fluorine position from the ideal oxygen site is very small, i.e., in all directions smaller than 0.018 Å. ^{19}F chemical shifts were calculated for both clusters. For the interstitial fluorine a value of +82 ppm is obtained, whereas the fluorine on the oxygen defect site has a value of −108 ppm. Comparison with experimental ^{19}F data (δ_{iso}= −113.9 ppm)

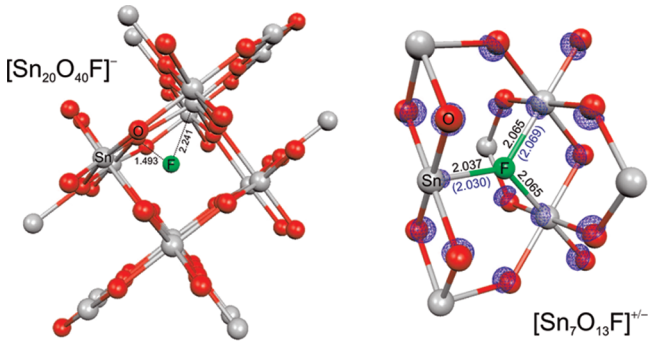

Figure 14. Relaxed structures of model clusters for interstitial (left) and O-defect sites (right); the right picture shows also an isosurface (blue chickenwire) of the electron density difference map, $\Delta\rho(r) = \rho_-(r) - \rho_+(r)$, between the negatively and positively charged ion at a value of 0.005; interatomic distances to F are given in Å (values in braces refer to $[Sn_7O_{13}F]^-$).

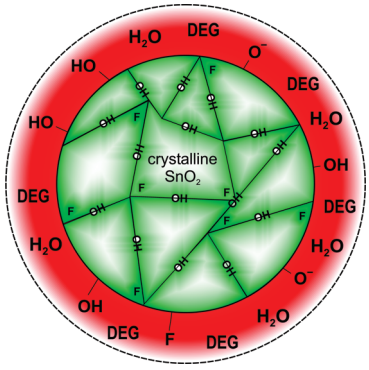

Figure 15. Model of a polycrystalline FTO-ap nanoparticle; within the SnO_2 crystallites F^- ions are inserted on oxygen sites (shading indicates a higher doping concentration near the grain boundaries); the charge is compensated at the intraparticle and outer surfaces; the latter is covered by a solvent layer consisting of DEG and water.

clearly rules out the interstitial site model (Figure 6) whereas good agreement with the substitution site model ($F_O^\bullet$) is obtained. Comparison of calculated and experimental anisotropic chemical shifts δ_{aniso} (Table 4) adds further confirmation, because the calculated anisotropic chemical shifts for F filling interstitial sites is significantly bigger than that of F on O-vacancies.

It is instructive to simulate what happens if two extra electrons are added to the $[Sn_7O_{13}F]^+$ cluster. Without allowing a structural relaxation, the excess electrons in $[Sn_7O_{13}F]^-$ are delocalized in the cluster (Figure 14) and the effect on the ^{19}F shift is small (−121 ppm). Delocalization of the extra electrons is what is expected in the standard semiconductor models.

Proposed Structural Model. In Figure 15, we sketch out a model for as-prepared SnO_2:F particles (FTO-ap) which is consistent with the aforementioned observations. The as-prepared SnO_2:F nanoparticles are polycrystalline. Their monocrystalline domains are approximately 2−4 nm in diameter (TEM, XRD and $^{119}Sn\{^1H\}$ C-REDOR-NMR). At the boundaries between different monocrystalline regions hydrogen atoms accumulate and fill the voids ($^{119}Sn\{^1H\}$ C-REDOR-NMR). F-atoms fill O-vacancies in the host structure (quantum chemical calculations, $^{119}Sn\{^{19}F\}-CP-NMR$) and do no exhibit clustering ($^{19}F-^{19}F$ 2D NMR correlation spectroscopy), still the

dx.doi.org/10.1021/cm103286t |Chem. Mater. 2011, 23, 1526–1538

distribution of F-atoms is not completely random and shows a preference to the intraparticle surfaces (comparison of ^{119}Sn-{^{1}H} C-REDOR and ^{19}F{^{1}H} C-REDOR-NMR). The electrons contributed by F-doping are localized at the intraparticle surface possibly in form of ionized surface defects (quantitative ^{119}Sn NMR and ^{119}Sn Mössbauer spectroscopy).

CONCLUSIONS

We have shown that nanoscale fluorine-doped SnO_2 with different doping levels can be prepared using the polyol approach. The prepared nanoparticles have a narrow size distribution and can be converted into an electrically conductive film which was obtained by first heating to 500 °C in air followed by 250 °C with forming gas (95% N_2/5% H_2). The resulting material shows an improved conductivity as compared to non-doped SnO_2 nanoparticles.

We rationalize these experimental findings on the basis of solid-state NMR and ^{119}Sn Mössbauer spectroscopy. We studied how F atoms are doped into the materials. Heteronuclear NMR experiments are introduced to characterize intraparticle interfaces in polycrystalline nanoparticles. Interestingly F doping is not directly related to an increase in charge carrier concentration in the final product, even though all evidence shows that F atoms do occupy O vacancy sites in SnO_2. Instead our data suggest that F helps to reduce the grain-boundary scattering mechanism, upon leaving the sample at elevated temperatures. Fluorine doped tin oxide nanoparticles are built up as shown in Figure 15.

In the course of this study we have presented new background compensated NMR 2D pulse-sequences and theoretical modeling of defect sites by the extended embedded ion method which we hope will find application in the context of other materials as well. An advantage of the latter method is that it allows to study the nature of diluted defects without having to fall back on an expensive supercell approach, which will include interaction of different defect sites to some extent.

ASSOCIATED CONTENT

Supporting Information. SEM and TEM images of FTO-ap (1.2 mol %), proposed locations of the F^- dopant in SnO_2 unit cell, partial structure optimizations of SnO_2:F, derivation of the $\sigma^{19F} \leftrightarrow \delta^{19F}$ conversion equation, and derivation of the ^{1}H surface occupancy. This material is available free of charge via the Internet at http://pubs.acs.org/.

AUTHOR INFORMATION

Corresponding Author
*E-mail: gunnej@cup.uni-muenchen.de.

ACKNOWLEDGMENT

E.H. and C.F. are grateful to W. Send and Prof. Dr. D. Gerthsen for performing TEM analysis. We also acknowledge the DFG Center for Functional Nanostructures (CFN) at the Karlsruhe Institute of Technology (KIT) for financial support. I. S. and R.P. gratefully acknowledge Deutsche Forschungsgemeinschaft for financial support at the University of Münster for Mössbauer spectroscopy analysis. J.S.a.d.G., J.W., and Y.S.A. gratefully acknowledge financial support through the Emmy-Noether program of the DFG (SCHM1570-2/1), Munich University (LMU), and the Leibnitz Rechenzentrum Garching (LRZ) for computational resources. We also thank C. Minke for technical support.

REFERENCES

(1) Granqvist, C. G.; Hultaker, A. *Thin Solid Films* **2002**, *411*, 1–5.
(2) Maier, J. *Festkörper - Fehler und Funktion*; Teubner: Leipzig, Germany, 2000.
(3) Chopra, K. L.; Major, S.; Pandya, D. K. *Thin Solid Films* **1983**, *102*, 1–46.
(4) Minami, T. *Semicond. Sci. Technol.* **2005**, *20*, S35–S44.
(5) Gordon, R. G. *MRS Bull.* **2000**, *25*, 52–57.
(6) Ginley, D. S.; Bright, C. *MRS Bull.* **2000**, *25*, 15–18.
(7) Lewis, B. G.; Paine, D. C. *MRS Bull.* **2000**, *25*, 22–27.
(8) Rakhshani, A. E.; Makdisi, Y.; Ramazaniyan, H. A. *J. Appl. Phys.* **1998**, *83*, 1049–1057.
(9) Klabunde, K. J. *Nanoscale Materials in Chemistry*; John, Wiley & Sons: New York, 2001.
(10) Street, R. A.; Wong, W. S.; Ready, S. E.; Chabinyc, M. L.; Arias, A. C.; Limb, S.; Salleo, A.; Lujan, R. *Mater. Today* **2006**, *4*, 32–37.
(11) Lee, D. H.; Chang, Y. J.; Herman, G. S.; Chang, C. H. *Adv. Mater.* **2007**, *19*, 843–847.
(12) Cushing, B. L.; Kolesnichenko, V. L.; O'Connor, C. J. *Chem. Rev.* **2004**, *104*, 3893–3946.
(13) Park, J.; Joo, J.; Kwon, S. G.; Jang, Y.; Hyeon, T. *Angew. Chem., Int. Ed.* **2007**, *46*, 4630–4660.
(14) Aegerter, M. A.; Mennig, M. *Sol−Gel Technologies for Glass Producers and Users*; Kluwer Academic Publishers: Boston, 2004.
(15) Livage, J.; Henry, M.; Sanchez, C. *Prog. Solid State Chem.* **1988**, *18*, 259–341.
(16) Mackenzie, J. D.; Bescher, E. P. *Acc. Chem. Res.* **2007**, *40*, 810–818.
(17) Destree, C.; Nagy, J. B. *Adv. Colloid Interface Sci.* **2006**, *123−126*, 353–367.
(18) Byrappa, K.; Adschiri, T. *Prog. Cryst. Growth Charact. Mater.* **2007**, *53*, 117–166.
(19) Demazeau, G. *J. Mater. Sci.* **2008**, *43*, 2104–2114.
(20) Fievet, F.; Lagier, J. P.; Figlarz, M. *MRS Bull.* **1989**, *14*, 29–34.
(21) Toneguzzo, P.; Viau, G.; Acher, O.; Guillet, F.; Bruneton, E.; Fievet-Vincent, F.; Fievet, F. *J. Mater. Sci.* **2000**, *35*, 3767–3784.
(22) Zhang, D. H.; Ma, H. L. *Appl. Phys. A: Mater. Sci. Process.* **1996**, *62*, 487–492.
(23) Ponce, M. A.; Castro, M. S.; Aldao, C. M. *J. Mater. Sci: Mater. Electron.* **2009**, *20*, 25–32.
(24) Savua, R.; Ponce, M. A.; Joannia, E.; Buenoa, P. R.; Castrob, M.; Cilensea, M.; Varelaa, J. A.; Longoa, E. *Mater. Res.* **2009**, *12*, 83–87.
(25) Schmidt-Rohr, K.; Rawal, A.; Fang, X.-W. *J. Chem. Phys.* **2007**, *126*, 054701.
(26) Roming, M.; Feldmann, C.; Avadhut, Y. S.; Schmedt auf der Günne, J. *Chem. Mater.* **2008**, *20*, 5787–5795.
(27) Lippens, P. E. *Phys. Rev. B* **1999**, *60*, 4576–4586.
(28) Mackenzie, K. J. D.; Smith, M. E. *Multinuclear Solid-State Nuclear Magnetic Resonance of Inorganic Materials*; Pergamon: Amsterdam, 2002.
(29) Weber, J.; Schmedt auf der Günne, J. *Phys. Chem. Chem. Phys.* **2010**, *12*, 583–603.
(30) Pickard, C. J.; Mauri, F. *Phys. Rev. B* **2001**, *63*, 245101–13.
(31) Lide, D. R. *CRC Handbook of Chemistry and Physics*, 86th ed.; CRC Press: Boca Raton, FL, 2005.
(32) Valdes, L. B. *Proc. IRE* **1952**, *40*, 445–448.
(33) Schmedt auf der Günne, J. *J. Magn. Reson.* **2003**, *165*, 18–32.
(34) Avadhut, Y. S.; Schneider, D.; Schmedt auf der Günne, J. *J. Magn. Reson.* **2009**, *201*, 1–6.
(35) Metz, G.; Wu, X. L.; Smith, S. O. *J. Magn. Reson. A* **1994**, *110*, 219–227.
(36) Gullion, T.; Schaefer, J. *J. Magn. Reson.* **1989**, *81*, 196–200.
(37) Chan, J. C. C.; Eckert, H. *J. Chem. Phys.* **2001**, *115*, 6095–6105.
(38) Chan, J. C. C. *Chem. Phys. Lett.* **2001**, *335*, 289–297.

(39) Brinkmann, A.; Levitt, M. H. *J. Chem. Phys.* **2001**, *115*, 357–384.
(40) Bak, M.; Rasmussen, J. T.; Nielsen, N. C. *J. Magn. Reson.* **2000**, *147*, 296–330.
(41) Vosegaard, T.; Malmendal, A.; Nielsen, N. C. *Monatsh. Chem.* **2002**, *133*, 1555–1574.
(42) Jeener, J.; Meier, B. H.; Bachmann, P.; Ernst, R. R. *J. Chem. Phys.* **1979**, *71*, 4546–4553.
(43) Brinkmann, A.; Schmedt auf der Günne, J.; Levitt, M. H. *J. Magn. Reson.* **2002**, *156*, 79–96.
(44) Bendall, M. R.; Gordon, R. E. *J. Magn. Reson.* **1983**, *53*, 365–385.
(45) ν_{rf} is the inverse of a duration of a pulse with 360° flip angle.
(46) Levitt, M. H.; Madhu, P. K.; Hughes, C. E. *J. Magn. Reson.* **2002**, *155*, 300–306.
(47) States, D. J.; Haberkorn, R. A.; Ruben, D. J. *J. Magn. Reson.* **1982**, *48*, 286–292.
(48) Under "QC", we comprehend the quantum mechanically treated region of the cluster.
(49) Frisch, M. J.; et al. *GAUSSIAN 03*, Revision D.01; Gaussian, Inc.: Wallingford, CT, 2004. (Full reference given in the Supporting Information).
(50) Glendering, E. D.; Badenhoop, J. K.; Reed, A. E.; Carpenter, J. E.; Bohmann, J. A.; Morales, C. M.; Weinhold, F. *NBO 5.0*; University of Wisconsin, Theoretical Chemistry Institute: Madison, WI, 2001.
(51) Adamo, C.; Barone, V. *J. Chem. Phys.* **1998**, *108*, 664–675.
(52) Ahlrichs, R.; May, K. *Phys. Chem. Chem. Phys.* **2000**, *2*, 943–945.
(53) Krishnan, R.; Binkley, J. S.; Seeger, R.; Pople, J. A. *J. Chem. Phys.* **1980**, *72*, 650–654.
(54) Wolinski, K.; Hinton, J. F.; Pulay, P. *J. Am. Chem. Soc.* **1990**, *112*, 8251–8260.
(55) Gamard, A.; Babot, O.; Jousseaume, B.; Rascle, M.-C.; Toupance, T.; Campet, G. *Chem. Mater.* **2000**, *12*, 3419–3426.
(56) Boegeat, D.; Jousseaume, B.; Toupance, T.; Campet, G.; Fournès, L. *Inorg. Chem.* **2000**, *39*, 3924–3927.
(57) Banerjee, A. N.; Maity, R.; Kundoo, S.; Chattopadhyay, K. K. *Phys. Status Solidi A* **2004**, *201*, 983–989.
(58) Biswas, P. K.; Dua, L.; De, A.; Chaudhuri, T. *Mater. Sci.* **2006**, *24*, 367–374.
(59) Hammarberg, E.; Prodi-Schwab, A.; Feldmann, C. *Thin Solid Films* **2008**, *516*, 7437–7442.
(60) Hammarberg, E.; Prodi-Schwab, A.; Feldmann, C. *J. Colloid Interface Sci.* **2009**, *334*, 29–36.
(61) Feldmann, C. *Adv. Funct. Mater.* **2003**, *13*, 101–107.
(62) Liang, H.; Yang, H.; Wang, W.; Li, J.; Xu, H. *J. Am. Chem. Soc.* **2009**, *131*, 6068–6069.
(63) Bühler, G.; Thölmann, D.; Feldmann, C. *Adv. Mater.* **2007**, *19*, 2224–2227.
(64) Feldmann, C. *Z. Anorg. Allg. Chem.* **2004**, *630*, 2473–2477.
(65) Bolzan, A. A.; Fong, C.; Kennedy, B. J.; Howard, C. J. *Acta Crystallogr., Sect. B* **1997**, *53*, 373–380.
(66) Feldmann, C.; Matschulo, S.; Ahlert, S. *J. Mater. Sci.* **2007**, *42*, 7076–7080.
(67) Kröger, F. A. *Chemistry of Imperfect Crystals*; North-Holland: Amsterdam, 1964.
(68) Kevane, C. J. *Phys. Rev.* **1964**, *133*, A1431–A1436.
(69) Agashe, C.; Major, S. S. *J. Mater. Sci.* **1996**, *31*, 2965–2969.
(70) Acosta, D. R.; Zironi, E. P.; Montoya, E.; Estrada, W. *Thin Solid Films* **1996**, *288*, 1–7.
(71) Wu, P.; Li, Q.; Zou, X.; Cheng, W.; Zhang, D.; Zhao, C.; Chi, L.; Xiao, T. *J. Phys. Conf. Ser.* **2009**, *188*, 012054.
(72) Mazzonea, A. M.; Morandi, V. *Eur. Phys. J. B* **2004**, *42*, 435–440.
(73) Lippens, P. E.; Olivier-Fourcade, J.; Jumas, J. C. *Hyperfine Interact.* **2000**, *126*, 137–141.
(74) Birchall, T.; Dénès, G.; Ruebenbauer, K.; Pannetier, J. *J. Chem. Soc., Dalton Trans.* **1981**, *12*, 2296–2299.
(75) Birchall, T.; Dénès, G.; Ruebenbauer, K.; Pannetier, J. *Hyperfine Interact.* **1986**, *29*, 1331–1334.
(76) Yanaga, M.; Endo, K.; Nakahara, H.; Ikuta, S.; Miura, T.; Takahashi, M.; Takeda, M. *Hyperfine Interact.* **1990**, *62*, 359–372.
(77) Gržeta, B.; Tkalčec, E.; Goebbert, C.; Takeda, M.; Takahashi, M.; Nomura, K.; Jakšić, M. *J. Phys. Chem. Solids* **2002**, *63*, 765–772.
(78) Jayakumar, O. D.; Sudarsan, V.; Kulshreshtha, S. K. *Physica B* **2007**, *392*, 67–71.
(79) Sougrati, M. T.; Jouen, S.; Hannoyer, B. *Hyperfine Interact.* **2006**, *167*, 815–818.
(80) Collins, G. S.; Kachnikowski, T.; Benczer-Koller, N.; Pasternak, M. *Phys. Rev. B* **1979**, *19*, 1369–1373.
(81) Cossement, C.; Darville, J.; Gilles, J. M.; Nagy, J. B.; Fernandez, C.; Amoureux, J. P. *Magn. Reson. Chem.* **1992**, *30*, 263–270.
(82) Knyrim, J. S.; Schappacher, F. M.; Pöttgen, R.; Schmedt auf der Günne, J.; Johrendt, D.; Huppertz, H. *Chem. Mater.* **2007**, *19*, 254–262.
(83) de Monredon, S.; Cellot, A.; Ribot, F.; Sanchez, C.; Armelao, L.; Gueneauc, L.; Delattre, L. *J. Mater. Chem.* **2002**, *12*, 2396–2400.
(84) Kreinbrink, A. T.; Sazavsky, C. D.; Pyrz, J. W.; Nelson, D. G. A.; Honkonen, R. S. *J. Magn. Reson.* **1990**, *88*, 267–276.
(85) Feike, M.; Demco, D. E.; Graf, R.; Gottwald, J.; Hafner, S.; Spiess, H. W. *J. Magn. Reson. A* **1996**, *122*, 214–221.
(86) Hohwy, M.; Jakobsen, H. J.; Edén, M.; Levitt, M. H.; Nielsen, N. C. *J. Chem. Phys.* **1998**, *108*, 2686–2694.
(87) Baur, W. H. *Acta Crystallogr.* **1956**, *9*, 515–520.